Indirect measurement of $\sin^2\theta_W$ (M_W) using $\mu^+\mu^-$ pairs from γ^*/Z-bosons produced in $p\bar{p}$ collisions at a center-of-momentum energy of 1.96 TeV

(The CDF Collaboration)

(Dated: November 4, 2013)

Drell-Yan lepton pairs are produced in the process $p\bar{p} \to \mu^+\mu^- + X$ through an intermediate γ^*/Z boson. The forward-backward asymmetry in the polar angle of the μ^- as a function of the invariant mass of the $\mu^+\mu^-$ pair is used to determine the effective-leptonic $\sin^2\theta_W$ ($\sin^2\theta^{\rm lept}_{\rm eff}$) from which the standard model electroweak-mixing parameter $\sin^2\theta_W$ is derived. The measurement sample, taken by the Collider Detector Facility (CDF) at the Fermilab Tevatron, corresponds to 9.2 fb^{-1} of integrated luminosity from $p\bar{p}$ collisions at a center-of-momentum energy of 1.96 TeV. The value of $\sin^2\theta^{\rm lept}_{\rm eff}$ is found to be 0.2315 ± 0.0010. When interpreted within the context of the standard model using the on-shell renormalization scheme ($\sin^2\theta_W = 1 - M_W^2/M_Z^2$), the measurement corresponds to $\sin^2\theta_W = 0.2233 \pm 0.0009$, or equivalently a W-boson mass of 80.365 ± 0.047 GeV/c^2. The value of the W-boson mass is in agreement with previous determinations in electron-positron collisions and at the Tevatron collider.

PACS numbers: 12.15.Lk, 13.85.Qk, 14.70.Hp

I. INTRODUCTION

The angular distribution of charged leptons ($l^\pm$) from the Drell-Yan [1] process is used to measure the electroweak-mixing parameter $\sin^2\theta_W$ [2]. At the Tevatron, Drell-Yan pairs are produced by the process $p\bar{p} \to l^+l^- + X$, where the l^+l^- pair is produced through an intermediate γ^*/Z boson, and X is the hadronic final state associated with the production of the boson. In the standard model, the Drell-Yan process at the Born level is described by two parton-level amplitudes:

$$q\bar{q} \to \gamma^* \to l^+l^-, \text{ and}$$
$$q\bar{q} \to Z \to l^+l^-.$$

The fermions (f) couple to the virtual photon via a vector coupling, $Q_f\gamma_\mu$, where Q_f is the fermion charge (in units of e). The fermion coupling to Z bosons consists of both vector (V) and axial-vector (A) couplings: $g_V^f\gamma_\mu + g_A^f\gamma_\mu\gamma_5$. The Born-level couplings are

$$g_V^f = T_3^f - 2Q_f \sin^2\theta_W$$
$$g_A^f = T_3^f,$$

where T_3^f is the third component of the fermion weak isospin. For positively (negatively) charged fermions, $T_3^f = \frac{1}{2}$ ($-\frac{1}{2}$). At the Born level or in all orders of the on-shell renormalization scheme, the $\sin^2\theta_W$ parameter is related to the W-boson mass M_W, and the Z-boson mass M_Z, by the relationship $\sin^2\theta_W = 1 - M_W^2/M_Z^2$. Beyond the Born level, weak-interaction radiative corrections modify the couplings into effective couplings. These effective couplings have been investigated at the Tevatron [3–5], at the LHC [6], and at LEP-1 and SLD [7]. Similar couplings have been investigated with neutrino-nucleon collisions at the Tevatron [8] and with electron-proton collisions at HERA [9].

In this article, the effective-leptonic $\sin^2\theta_W$, or $\sin^2\theta^{\rm lept}_{\rm eff}$, is derived from a measurement of the forward-backward asymmetry in the l^- polar angle as a function of the lepton-pair invariant mass. Section II provides an overview of the lepton angular distributions and the extraction of $\sin^2\theta^{\rm lept}_{\rm eff}$. Section III discusses quantum chromodynamics (QCD) calculations for the forward-backward asymmetry, and how the electroweak radiative-correction form factors used in the analysis of high-energy e^+e^- collisions are incorporated into the calculations. These form factors are important in determining $\sin^2\theta_W$ from the measurement of $\sin^2\theta^{\rm lept}_{\rm eff}$. Section IV describes the experimental apparatus. Section V reports on the selection of muons and muon pairs for the measurement of the forward-backward asymmetry. Section VI describes the simulation of the reconstructed data. Section VII presents the measurement of the asymmetry and the corrections made to both the data and simulation. Section VIII describes the method used to extract $\sin^2\theta^{\rm lept}_{\rm eff}$. Section IX describes the systematic uncertainties. Finally, Sec. X gives the results, and Sec. XI the summary. The units $\hbar = c = 1$ are used for equations and symbols, but standard units are used for numerical values.

II. LEPTON ANGULAR DISTRIBUTIONS

The angular distribution of leptons in the boson rest frame is governed by the polarization state of the γ^*/Z boson. In amplitudes at higher order than tree level, initial-state QCD interactions of the colliding partons impart transverse momentum, relative to the collision axis, to the γ^*/Z boson. This affects the polarization states.

The polar and azimuthal angles of the l^- in the rest frame of the boson are denoted as ϑ and φ, respectively. For this analysis, the ideal positive-z axis coincides with

the direction of the incoming quark so that ϑ parallels the definition used in e^+e^- collisions at LEP [7]. This frame is approximated by the Collins-Soper (CS) rest frame [10] for $p\bar{p}$ collisions. The CS frame is reached from the laboratory frame via a Lorentz boost along the laboratory z axis into a frame where the z component of the lepton-pair momentum is zero, followed by a boost along the transverse momentum of the pair. The transverse momentum ($P_{\rm T}$) in a reference frame is the magnitude of momentum transverse to the z axis. Within the CS frame, the z axis for the polar angle is the angular bisector between the proton direction and the negative of the anti-proton direction. The x axis for the azimuthal angle is the direction of the lepton-pair $P_{\rm T}$. By construction, the CS-frame angles ϑ and φ are invariant with respect to boosts along the $p\bar{p}$ collision axis. At $P_{\rm T} = 0$, the CS and laboratory coordinate-system axes are the same, and if the incoming quark of the Drell-Yan parton amplitude is from the proton, the z axis and quark directions coincide.

The general structure of the Drell-Yan lepton angular distribution in the boson rest frame consists of nine helicity cross-section ratios [11],

$$\begin{aligned}\frac{dN}{d\Omega} \propto\ & (1+\cos^2\vartheta) + \\ & A_0\,\frac{1}{2}\,(1-3\cos^2\vartheta) + \\ & A_1\,\sin 2\vartheta\cos\varphi + \\ & A_2\,\frac{1}{2}\,\sin^2\vartheta\cos 2\varphi + \\ & A_3\,\sin\vartheta\cos\varphi + \\ & A_4\,\cos\vartheta + \\ & A_5\,\sin^2\vartheta\sin 2\varphi + \\ & A_6\,\sin 2\vartheta\sin\varphi + \\ & A_7\,\sin\vartheta\sin\varphi\,. \end{aligned} \tag{1}$$

The A_{0-7} coefficients are the ratios of the helicity cross sections for boson production relative to unpolarized production, and are functions of kinematic variables of the boson. They vanish at $P_{\rm T} = 0$, except for A_4 which is present at the tree level of QCD and is responsible for the forward-backward l^- asymmetry in $\cos\vartheta$. Thus, for $P_{\rm T} = 0$, the angular distribution reduces to the tree-level form $1 + \cos^2\vartheta + A_4\cos\vartheta$. The A_4 coefficient is relatively uniform across the range of transverse momentum where the cross section is large, but slowly drops for larger values of $P_{\rm T}$ where the cross section is very small. The A_{5-7} coefficients appear at second order in the QCD strong coupling, α_s, and are small in the CS frame [11]. Hereafter, the angles (ϑ, φ) and the angular coefficients A_{0-7} are specific to the CS rest frame.

The $A_4\cos\vartheta$ term is parity violating, and is due to the interference of the amplitudes of the vector and axial-vector currents. Its presence adds an asymmetry to the φ-integrated $\cos\vartheta$ cross section. Two sources contribute: the interference between the Z-boson vector and axial-vector amplitudes, and the interference between the photon vector and Z-boson axial-vector amplitudes. The asymmetric component from the γ-Z interference cross section is proportional to g_A^f. The asymmetric component from Z boson self-interference has a coupling factor that is a product of g_V^f from the lepton and quark vertices, and thus is related to $\sin^2\theta_W$. At the Born level, this product is

$$T_3^l\,(1-4|Q_l|\sin^2\theta_W)\,T_3^q\,(1-4|Q_q|\sin^2\theta_W),$$

where l and q denote the lepton and quark, respectively. For the Drell-Yan process, the quarks are predominantly light quarks: u, d, or s. As $\sin^2\theta_W \approx 0.223$, the coupling factor has an enhanced sensitivity to $\sin^2\theta_W$ at the lepton-Z vertex. A 1% variation in $\sin^2\theta_W$ changes the lepton factor (containing Q_l) by $\approx 8\%$, while the quark factor (containing Q_q) changes by $\approx 1.5\%$ for the u quark, and $\approx 0.4\%$ for the d and s quarks. Electroweak-radiative corrections do not drastically alter this Born-level interpretation. Loop and vertex electroweak-radiative corrections are multiplicative form-factor corrections to the couplings that change their value by a few percent.

For the description of the Drell-Yan process, the rapidity, transverse momentum, and mass of a particle are denoted as y, $P_{\rm T}$, and M, respectively. The energy and momentum of particles are denoted as E and P, respectively. In a given coordinate frame, the rapidity is $y = \frac{1}{2}\,\ln[\,(E+P_{\rm z})/(E-P_{\rm z})\,]$, where $P_{\rm z}$ is the component of momentum along the z axis of the coordinate frame.

The l^- forward-backward asymmetry in $\cos\vartheta$ is defined as

$$A_{\rm fb}(M) = \frac{\sigma^+(M) - \sigma^-(M)}{\sigma^+(M) + \sigma^-(M)} = \frac{3}{8}A_4(M)\,, \tag{2}$$

where M is the lepton-pair invariant mass, σ^+ is the total cross section for $\cos\vartheta \geq 0$, and σ^- is the cross section for $\cos\vartheta < 0$. The $\sin^2\theta_{\rm eff}^{\rm lept}$ parameter is derived from the experimental measurement of $A_{\rm fb}(M)$ and predictions of $A_{\rm fb}(M)$ for various input values of $\sin^2\theta_W$. The prediction that best describes the measured $A_{\rm fb}(M)$ provides the derived value of $\sin^2\theta_{\rm eff}^{\rm lept}$. Electroweak and QCD radiative corrections are included in the predictions of $A_{\rm fb}(M)$. The QCD predictions for $A_{\rm fb}(M)$ contain an implementation of electroweak radiative corrections derived from an approach adopted at LEP [12].

III. ENHANCED QCD PREDICTIONS

Drell-Yan process calculations with QCD radiation do not typically include the full electroweak-radiative corrections. However, the QCD, quantum electrodynamic (QED), and weak corrections can be organized to be individually gauge invariant so that they can be applied separately and independently.

QED radiative corrections with photons in the final state are not included in the calculation of $A_{\rm fb}$. Instead, they are applied in the physics and detector simulation

of the Drell-Yan process used in the measurement of $A_{\rm fb}$. For the process $q\bar{q} \to l^+l^-$, QED final-state radiation is most important, and is included. The effects of QED radiative corrections are removed from the measurement of $A_{\rm fb}$.

The Drell-Yan process and the production of quark pairs in high energy e^+e^- collisions are analog processes: $q\bar{q} \to e^+e^-$ and $e^+e^- \to q\bar{q}$. At the Born level, the process amplitudes are of the same form except for the interchange of the electron and quark labels. Electroweak radiative corrections, calculated and extensively used for precision fits of LEP-1 and SLD measurements to the standard model [7], can be applied to the Drell-Yan process.

In the remainder of this section, the technique used to incorporate independently calculated electroweak radiative corrections for e^+e^- collisions into existing QCD calculations for the Drell-Yan process is presented.

A. Electroweak radiative corrections

The effects of virtual electroweak radiative corrections are incorporated into Drell-Yan QCD calculations via form factors for fermion-pair production in e^+e^- collisions, $e^+e^- \to Z \to f\bar{f}$. The Z-amplitude form factors are calculated by ZFITTER 6.43 [12], which is used with LEP-1 and SLD measurement inputs for precision tests of the standard model [7]. It is a semi-analytical calculation for fermion-pair production and radiative corrections for high-energy e^+e^- collisions. Corrections to fermion-pair production via the virtual photon include weak-interaction W-boson loops in the photon propagator and Z propagators at fermion-photon vertices; these corrections are not gauge invariant except when combined with their gauge counterparts in the Z amplitude. The ZFITTER weak and QED corrections are organized to be separately gauge invariant. Consequently, weak corrections to fermion-pair production via the virtual photon are included with the Z-amplitude form factors. The renormalization scheme used by ZFITTER is the on-shell scheme [13], where particle masses are on-shell, and

$$\sin^2\theta_W = 1 - M_W^2/M_Z^2 \qquad (3)$$

holds to all orders of perturbation theory by definition. Since the Z-boson mass is accurately known (to ± 0.0021 GeV/c^2 [7]), the inference of $\sin^2\theta_W$ is equivalent to an indirect W-boson mass measurement.

Form factors calculated by ZFITTER are stored for later use in QCD calculations. The specific standard-model assumptions and parameters used in the form-factor calculation are presented in Appendix A. The calculated form factors are ρ_{eq}, κ_e, κ_q, and κ_{eq}, where the label e denotes an electron, and q a quark. As the calculations use the massless-fermion approximation, the form factors only depend on the charge and weak isospin of the fermions. Consequently, the stored form factors are distinguished by three labels: e (electron type), u (up-quark type), and d (down-quark type). The form factors are complex valued, and functions of the $\sin^2\theta_W$ parameter and the Mandelstam s variable of the $e^+e^- \to Z \to f\bar{f}$ process. The first three form factors are important. They modifiy the Born-level g_A^f and g_V^f couplings:

$$g_V^f \to \sqrt{\rho_{eq}}\,(T_3^f - 2Q_f\kappa_f\,\sin^2\theta_W), \text{ and}$$
$$g_A^f \to \sqrt{\rho_{eq}}\,T_3^f,$$

where $f = e$ or q.

The combination $\kappa_f \sin^2\theta_W$, called an effective-mixing parameter, is directly accessible from measurements of the asymmetry in the $\cos\vartheta$ distribution. However, neither the $\sin^2\theta_W$ parameter nor the form factors can be inferred from experimental measurements without the standard model. The effective-mixing parameters are denoted as $\sin^2\theta_{\rm eff}$ to distinguish them from the on-shell definition of $\sin^2\theta_W$ (Eq. (3)). The Drell-Yan process is most sensitive to the parameter $\sin^2\theta_{\rm eff}$ of the lepton vertex, or $\kappa_e \sin^2\theta_W$, which is commonly denoted as $\sin^2\theta_{\rm eff}^{\rm lept}$. At the Z pole, κ_e is independent of the quark type. For comparisons with other measurements, the value of $\sin^2\theta_{\rm eff}^{\rm lept}$ at the Z pole $\mathrm{Re}\,\kappa_e(s_Z)\sin^2\theta_W$ ($s_Z = M_Z^2$), is used.

B. QCD calculations

The Drell-Yan QCD calculations are improved by incorporating the ZFITTER form factors into the process amplitude. This provides an enhanced Born approximation (EBA) to the electroweak terms of the amplitude. The QED photon self-energy correction is included as part of the EBA. The photon amplitude influences the shape of $A_{\rm fb}$ away from the Z pole via its interference with the axial-vector part of the Z amplitude. The γ-Z interference, whose cross section is proportional to $(s - M_Z^2)$, begins to dominate the total-interference cross section away from the Z pole. As it dilutes measurements of $\sin^2\theta_{\rm eff}$, photonic corrections are also included.

The ZFITTER form factors, ρ_{eq}, κ_e, and κ_q are inserted into the Born g_A^f and g_V^f couplings for the Drell-Yan process. The κ_{eq} form factor is incorporated as an amplitude correction. Complex-valued form factors are used in the amplitude. Operationally, only the electroweak-coupling factors in the QCD cross sections are affected. The standard LEP Z-boson resonant line shape and the total-decay width calculated by ZFITTER are used.

A leading-order (LO) QCD or tree calculation of $A_{\rm fb}$ for the process, $p\bar{p} \to \gamma^*/Z \to l^+l^-$, is used as the baseline EBA calculation with ZFITTER form factors. It is used to provide a reference for the sensitivity of $A_{\rm fb}$ to QCD radiation. The CT10 [14] next-to-leading-order (NLO) parton distribution functions (PDF) provide the incoming parton flux used in all QCD calculations discussed in this section except where specified otherwise.

Two NLO calculations, RESBOS [15] and the POWHEG-BOX framework [16], are modified to be EBA-based QCD

calculations. For both calculations, the boson $P_{\rm T}^2$ distribution is finite as $P_{\rm T}^2$ vanishes. The RESBOS calculation combines a NLO fixed-order calculation at high boson-$P_{\rm T}$ with the Collins-Soper-Sterman resummation formalism [17] at low boson-$P_{\rm T}$, which is an all-orders summation of large terms from gluon emission. The RESBOS calculation uses CTEQ6.6 [18] NLO PDFs. The POWHEG-BOX is a fully unweighted partonic-event generator that implements Drell-Yan production of l^+l^--pairs at NLO. The NLO production implements a Sudakov form factor that controls the infrared diverence at low $P_{\rm T}$, and is constructed to be interfaced with parton showering to avoid double counting. The PYTHIA 6.41 [19] parton-showering algorithm is used to produce the final hadron-level event.

The RESBOS and POWHEG-BOX NLO calculations are similar and consistent. The RESBOS calculation is chosen as the default EBA-based QCD calculation of $A_{\rm fb}$ with various input values of $\sin^2\theta_W$. As the POWHEG-BOX NLO program has a diverse and useful set of calculation options, it is used to estimate QCD systematic uncertainties.

IV. THE EXPERIMENTAL APPARATUS

The CDF experimental apparatus is a general-purpose detector [20] at the Fermilab Tevatron $p\bar{p}$ collider whose center-of-momentum (cm) energy is 1.96 TeV. The positive z-axis is directed along the proton direction. For particle trajectories, the polar angle $\theta_{\rm cm}$ is relative to the proton direction and the azimuthal angle $\phi_{\rm cm}$ is oriented about the beamline axis with $\pi/2$ being vertically upwards. The component of the particle momentum transverse to the beamline is $P_{\rm T} = P\sin\theta_{\rm cm}$. The pseudorapidity of a particle trajectory is $\eta = -\ln\tan(\theta_{\rm cm}/2)$. Detector coordinates are specified as $(\eta_{\rm det}, \phi_{\rm cm})$, where $\eta_{\rm det}$ is the pseudorapidity relative to the detector center $(z = 0)$.

The central charged-particle tracking-detector (tracker) is a 3.1 m long, open-cell drift chamber [21] that radially extends from 0.4 to 1.4 m. Between the Tevatron beam pipe and the central tracker is a 2 m long silicon vertex-tracker [22]. Both trackers are immersed in a 1.4 T axial magnetic field. Outside the central tracker is a central barrel calorimeter [23, 24] that covers the region $|\eta_{\rm det}| < 1.1$. The forward end-cap regions are covered by the end-plug calorimeters [25–27] that cover the regions $1.1 < |\eta_{\rm det}| < 3.5$.

The muon detectors are outer charged-particle trackers that are positioned behind hadron absorbers. The primary absorbers are the calorimeters. There are four separate detectors, labeled CMU, CMP, CMX, and BMU. The CMU muon detector [28], located just beyond the central barrel calorimeter, has a cylindrical geometry, and covers the region $|\eta_{\rm det}| < 0.6$. The central calorimeter provides approximately 5.5 pion absorption lengths of shielding. The CMP muon detector shadows the CMU detector and covers the same region, $|\eta_{\rm det}| < 0.6$. It has a rectangular geometry, and there is an additional 2.3 pion absorption lengths of shielding between the CMP and CMU detectors. The CMX muon detectors cover the regions $0.6 < |\eta_{\rm det}| < 1$, and are located behind approximately 6.2 pion absorption lengths of shielding. The BMU muon detectors cover the forward regions $1 < |\eta_{\rm det}| < 1.5$, and are situated behind at least 6.2 pion absorption lengths of shielding.

V. DATA SELECTION

The data set, collected over 2002-2011, consists of 9.2 fb^{-1} of $p\bar{p}$ collisions at a center-of-momentum energy of 1.96 TeV. Section V A reports on the online selection of events for the $A_{\rm fb}$ measurement. Section V B describes the offline selection of muon candidates, and Sec. V C the selection of muon pairs.

A. Triggers

Muon candidates used in this analysis are selected from two online triggers: CMUP_18 and CMX_18 [29–32]. These selections require at least one muon candidate in the event to be in the region $|\eta_{\rm det}| < 1$. The CMUP_18 selection accepts muon candidates with a $P_{\rm T} > 18$ GeV/c track in the central tracker that is matched to tracks in both the CMU and CMP muon detectors. The CMX_18 selection accepts muon candidates with a $P_{\rm T} > 18$ GeV/c track in the central tracker that is matched to a track in the CMX muon detector.

B. Muon Selection

The offline muon selection criteria is more stringent than the online criteria. The selection begins with a charged-particle track candidate (*track*) in the central tracker. The track is extrapolated through the calorimeters and into the muon detectors for association with independent track *segments* reconstructed in the muon detectors. The selection is based on the track quality, energy deposition in the calorimeters, and the track-to-segment matching. The energy deposition in the calorimeters must be consistent with that of a minimum-ionizing particle. The track-to-segment matching is applied only if the track extrapolates into a fiducial region of a muon detector. The selection criteria used [20] are stringent and delivers a well reconstructed sample of muon candidates with very high purity.

The category of muon candidates with associated segments in a muon detector are denoted with these labels: CMUP, CMU, CMP, CMX, and BMU. For the CMUP category, the track extrapolation has matching segments in both the CMU and CMP detectors. The CMU category has a matching segment in the CMU detector but not the CMP. The CMP category has a matching segment

in the CMP detector but not the CMU; this category is rare. The CMX and BMU categories have matching segments in the CMX and BMU muon detectors, respectively.

As the CDF muon detectors have gaps in their coverage, muon candidates without associated segments in a muon detector are also used. They consist of tracks extrapolating into muon-detector non-fiducial regions, and fiducial tracks without matching segments. This category is denoted as CMIO (minimum-ionizing category). The muon candidate is only required to satisfy the track quality and minimum-ioniziation energy loss requirement in the calorimeters.

The acceptance of muon candidates is limited by the geometrical acceptance of the central tracker, whose acceptance of tracks is flat up to $|\eta| \sim 1.1$ then falls rapidly and vanishes at $|\eta| \sim 1.5$. In the $|\eta| > 1.1$ region, track quality requirements for BMU category muons are relaxed. However, track quality requirements for CMIO muons which have no associated muon detector segments are kept stringent.

C. Muon Pair Selection

Events are required to contain two muon candidates. The kinematic and fiducial acceptance region for muons and muon pairs used in the $A_{\rm fb}$ measurement are listed below.

1. Muon kinematics and fiducial regions
   - $P_{\rm T} > 20$ GeV/c
   - Muon 1: CMUP or CMX category
   - Muon 2: any muon category
2. Muon-pair kinematics
   - Muon 1 and 2 are oppositely charged
   - $|y| < 1$
   - $M > 40$ GeV/c^2

One of the muons, denoted by "Muon 1", is a CMUP or CMX category muon that is consistent with the online selection. As the second muon can be any one of the six muon categories, there are eleven muon-pair topologies based on the muon categories. Muon pairs consistent with the passage of cosmic rays through the detector are rejected [20]. The limited acceptance of the central tracker restricts the accepted rapidities of the muon pairs. As there is very limited acceptance for $|y| > 1$, the $A_{\rm fb}$ measurement is only for the kinematic region of $|y| < 1$.

The numbers of events passing all requirements and after background subtraction is 276 623. The event count for the various muon pair topologies is summarized in Table I. As the two topologies with CMP-category muons are rare, they are combined. The backgrounds are from QCD and the electroweak (EWK) processes of WW, WZ, ZZ, $t\bar{t}$, W+jets, and also $Z \to \tau^+\tau^-$. The QCD background is primarily from dijets where a particle in a jet has penetrated the shielding. The high-$P_{\rm T}$ muon sources have at least one real muon. The second muon is either a real second muon or a fake one. The QCD backgrounds are estimated with the number of same charge muon pairs in the sample, and amount to 0.10%. The EWK backgrounds are derived from PYTHIA [33] samples with detector simulation, and amount to 0.53%. The muon-pair invariant mass distribution for the data and the backgrounds are shown in Fig. 1. Backgrounds are subtracted in the measurement of $A_{\rm fb}$.

TABLE I. The number of events after background subtraction for the various muon-pair topologies. The event counts are rounded to the nearest integer.

Muon 1	Muon 2	Events
CMUP	CMUP	43 900
CMUP	CMX	69 704
CMUP	CMU	18 652
CMUP	CMIO	50 122
CMUP	BMU	15 774
CMX	CMX	26 317
CMX	CMU	14 360
CMX	CMIO	30 752
CMX	BMU	6 823
CMUP+CMX	CMP	448

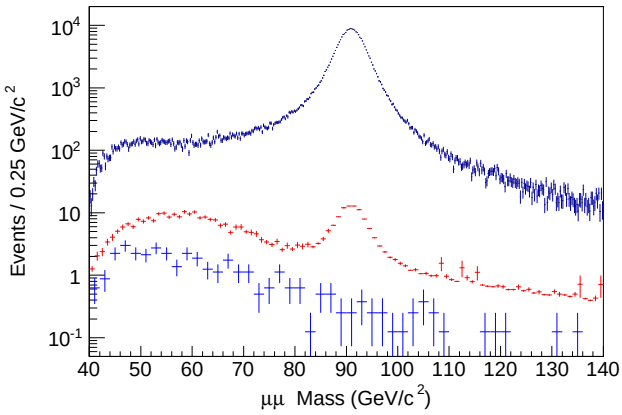

FIG. 1. Muon-pair invariant mass distributions. The upper set of crosses is the background subtracted data, the middle set of crosses is the EWK background, and the lower set of crosses is the QCD background (same charge muon pairs).

VI. DATA SIMULATION

Drell-Yan pair production is simulated using the Monte Carlo event generator, PYTHIA [33], and CDF II detector-simulation programs. PYTHIA generates the hard, leading-order QCD interaction, $q + \bar{q} \to \gamma^*/Z$, simulates initial-state QCD radiation via its parton-shower algorithms, and generates the decay $\gamma^*/Z \to l^+l^-$. The

CTEQ5L [34] nucleon parton-distribution functions are used in the QCD calculations. The underlying event and boson $P_{\rm T}$ parameters are from PYTHIA tune AW (i.e., PYTUNE 101, which is a tuning to previous CDF data) [33, 35, 36]. The generator-level $P_{\rm T}$ distribution is adjusted further so that the shape of the reconstruction-level, simulated $P_{\rm T}$ distribution is the same as in the data.

Generated events are processed by the CDF event and detector simulation. The event simulation includes PHOTOS 2.0 [37, 38], which adds final-state QED radiation (FSR) to decay vertices with charged particles (e.g. $\gamma^*/Z \to \mu\mu$). The default implementation of PYTHIA plus PHOTOS (PYTHIA+PHOTOS) QED radiation in the CDF data-simulation infrastructure has been validated by a previous measurement of $\sin^2\theta^{\rm lept}_{\rm eff}$ using Drell-Yan electron pairs [5].

The time-dependent beam and detector conditions for data runs recorded and used for physics analyses are simulated. The beam conditions simulated are the p and $\bar{p}$ beamline parameters, the $p\bar{p}$ luminous region profile, and the instantaneous and integrated luminosities per run. The detector conditions simulated are detector component calibrations, which include channel gains and malfunctions. The simulated events are reconstructed, selected, and analyzed as the data.

VII. THE $A_{\rm fb}$ MEASUREMENT

The Collins-Soper frame angle, $\cos\vartheta$ [10], is reconstructed using the following laboratory-frame quantities: the lepton energies (E), the lepton momenta along the beam line (P_z), the dilepton invariant mass (M), and the dilepton transverse momentum ($P_{\rm T}$). The angle of the negatively-charged lepton is

$$\cos\vartheta = \frac{l^-_+ l^+_- - l^-_- l^+_+}{M\sqrt{M^2+P^2_{\rm T}}}\,,$$

where $l_\pm = (E \pm P_z)$ and the $+$ $(-)$ superscript specifies that $l_\pm$ is for the positively (negatively) charged lepton. Similarly, the Collins-Soper expression for φ in terms of laboratory-frame quantities is

$$\tan\varphi = \frac{\sqrt{M^2+P^2_{\rm T}}}{M}\,\frac{\vec{\Delta}\cdot\widehat{R}_{\rm T}}{\vec{\Delta}\cdot\widehat{P}_{\rm T}}\,,$$

where $\vec{\Delta}$ is the difference between the l^- and l^+ momentum vectors, $\widehat{R}_{\rm T}$ is the transverse unit vector along $\vec{P}_p \times \vec{P}$, with $\vec{P}_p$ being the proton momentum vector and $\vec{P}$ the lepton-pair momentum vector, and $\widehat{P}_{\rm T}$ is the unit vector along the transverse component of the lepton-pair momentum vector. When $P_{\rm T} = 0$, the angular distribution is azimuthally symmetric.

The $A_{\rm fb}$ is measured in 16 mass bins, starting with $M = 50$ GeV/c^2. This section details the measurement method, the corrections to the data and the simulation, and presents the fully corrected measurement. The key components of the measurement are introduced in the next two sections: Section VII A describes the newly developed event-weighting technique used for the measurement, and Section VII B describes the muon momentum and resolution calibration. Section VII C describes the data-driven corrections applied to the simulated data that are needed for the measurement. Section VII D describes the resolution unfolding technique and the corresponding covariance matrix of the unfolded $A_{\rm fb}$ measurement. Section VII E describes the final corrections to the measurement and presents the fully corrected measurement of $A_{\rm fb}$.

A. Event-Weighting Method

The forward-backward asymmetry $A_{\rm fb}$ (Eqn. (2)) is typically determined in terms of the measured cross section $\sigma = N/(\mathcal{L}\,\epsilon A)$, where N the number of observed events, $\mathcal{L}$ is the integrated luminosity, ϵ the reconstruction efficiency, and A the acceptance within the kinematic and fiducial restrictions. The expression is

$$A_{\rm fb} = \frac{N^+/(\epsilon A)^+ - N^-/(\epsilon A)^-}{N^+/(\epsilon A)^+ + N^-/(\epsilon A)^-}\,.$$

The terms $N^{+(-)}$ and $(\epsilon A)^{+(-)}$ respectively represent the N and ϵA for $\cos\vartheta \geq 0$ ($\cos\vartheta < 0$). Each muon pair topology listed in Table I requires separate evaluations of $(\epsilon A)^{\pm}$. This is extremely challenging to accomplish.

The $A_{\rm fb}$ is measured using a new and simpler technique: the *event-weighting* method [39]. The method is equivalent to measurements of $A_{\rm fb}$ in $|\cos\vartheta|$ bins with these simplifying assumptions:

- $(\epsilon A)^+ = (\epsilon A)^-$ in each $|\cos\vartheta|$ bin, and
- Eqn. (1) describes lepton angular distributions.

The measurement of $A_{\rm fb}$ within a $|\cos\vartheta|$ bin ($A'_{\rm fb}$) only depends on $N^{\pm}$, but there is an angular dependence,

$$A'_{\rm fb} = \frac{N^+ - N^-}{N^+ + N^-} \propto A_{\rm fb}\frac{|\cos\vartheta|}{1+\cos^2\vartheta+\cdots}\,, \qquad (4)$$

where $1+\cos^2\vartheta+\cdots$ denotes symmetric terms in Eqn. (1). The numerator difference contributes the $|\cos\vartheta|$ term, and the denominator sum the $1+\cos^2\vartheta+\cdots$ term. As the angular factor is the equivalent of an importance sampling factor, the binned measurements are reformulated into an unbinned, event-by-event weighted expression

$$A_{\rm fb} = \frac{N^+_n - N^-_n}{N^+_d + N^-_d}\,. \qquad (5)$$

The $N^{\pm}_n$ and $N^{\pm}_d$ terms represent weighted event counts, and the subscripts n and d signify the numerator and denominator sums, respectively, which contain the same

events but with different event weights. The weights remove the angular terms of the numerator and denominator sums, and include a statistical factor for the expected measurement uncertainty at each value of $|\cos\vartheta|$ (the inverse of the square of the angular factor in $A'_{\rm fb}$). Consequently, the method is equivalent to using a maximum-likelihood technique, and the statistical precision of the $A_{\rm fb}$ is expected to be about 20% better relative to the direct counting evaluation.

The event weights are functions of the reconstructed kinematic variables, $\cos\vartheta$, φ, and the muon-pair variables, M and $P_{\rm T}$. Only the A_0 and A_2 terms of Eqn. (1) are used in the denominator of the angular factor of Eqn. (4), and the angular coefficients are parameterized with

$$A_0 = A_2 = \frac{kP_{\rm T}^2}{kP_{\rm T}^2 + M^2}$$

where k is a tuning-factor for the $P_{\rm T}$ dependence of the A_0 and A_2 coefficients. For this analysis, $k = 1.65$, which is derived from a previous measuremement of angular coefficients [40]. The inclusion of these angular terms within the event weights has very little impact on $A_{\rm fb}$ because the bulk of the events are at low boson $P_{\rm T}$.

The event-weighting method does not compensate the following:

- smearing of kinematic variables due to the detector resolution,
- kinematic regions with limited acceptance, and
- detector non-uniformity, $(\epsilon A)^+ \neq (\epsilon A)^-$.

These require separate and additional compensation. Resolution smearing effects are unfolded with the aid of the data simulation. For the unfolding to be accurate, the muon momentum scale and resolution for both the data and simulated data are precisely calibrated. In addition, the $\cos\vartheta$ and muon-pair invariant mass distributions of the simulated data are matched to agree with the data.

After resolution unfolding, the event-weighted $A_{\rm fb}$ can have a small, second-order bias. The bias is estimated using the simulation, and is the difference between the true value of $A_{\rm fb}$ from the underlying events generated by PYTHIA and the simulated $A_{\rm fb}$ measurement. One source of bias is from the limited muon-pair acceptance in its rapidity y. The forward-backward asymmetry has a slight y dependence: There is a modest increase in $A_{\rm fb}$ with increasing $|y|$ for $|y| \sim 1$ and above. In regions of very limited or no acceptance, the event-weighted $A_{\rm fb}$ contains little or no contributions from those regions. This is the reason for the kinematic acceptance restriction of $|y| < 1$ specified in Sec. V C. Another potential source of bias is from detector non-uniformity: $(\epsilon A)^+ \neq (\epsilon A)^-$. The effects of these biases, which are quantified later in Sec. VII E, are removed from the $A_{\rm fb}$ measured with the data.

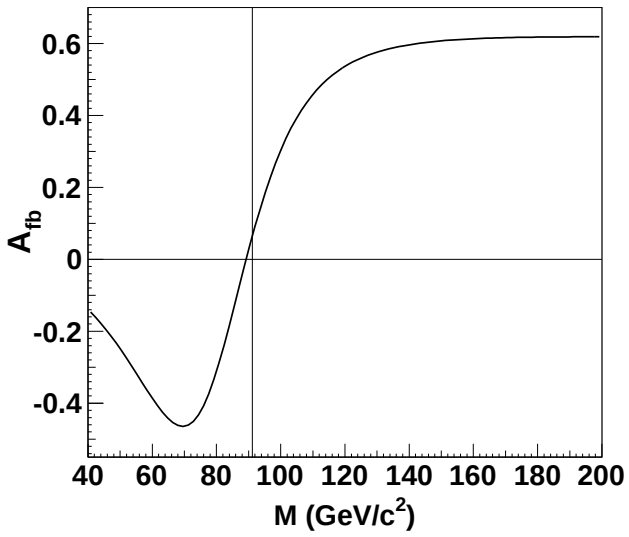

FIG. 2. The typical behavior of $A_{\rm fb}$ as a function of the lepton-pair invariant mass. The vertical line is at $M = M_Z$.

B. Muon Momentum Calibration

The typical behavior of $A_{\rm fb}$ as a function of the lepton-pair invariant mass is shown in Fig. 2. With momentum mis-calibrations, an event produced at mass M with the asymmetry $A_{\rm fb}(M)$ is associated a different mass M'. The measured $A_{\rm fb}(M')$ becomes biased because of this systematic dilution. The correct calibration of the muon momentum is critical for the measurement of $A_{\rm fb}(M)$.

The momentum calibration procedure is adapted from a technique developed for CMS [41]. The CMS technique is briefly described next, and then followed by the CDF adaptation. The CMS tracker is split into regions of (η, ϕ). For each region, track curvature corrections are determined. They are the curvature scale correction to $\int \mathbf{B}\cdot\mathbf{dl}$ and the tracking alignment offset, which are denoted by $1 + s$ and o, respectively. The corrections are the same for positively and negatively charged particles. For an input track curvature C, the corrected curvature is $(1+s)\,C+o$. In the following discussion, the curvature C is synonymous to the charge-signed $1/P_{\rm T}$ of a track.

The calibration sample consists of oppositely-charged muon pairs from the Z-boson region. The muons in the sample are binned according to their (η, ϕ) trajectories, which for CMS is the same as a tracker (η, ϕ) region. The charge-signed $1/P_{\rm T}$ for the $\mu^\pm$ is denoted by $C^\pm$, and these distributions in each bin have sharp peaks. The peaks get narrower as the Z-boson mass selection window is made smaller. The calibration method requires a single distinct peak in the $C^\pm$ distributions. The locations of these peaks are calibrated against simulated Drell-Yan muon-pair events that pass the calibration sample selection criteria. The calibration ansatz is that the $1 + s$ and o parameters map the peaks for $C^\pm$ onto the true positions predicted by the simulation. The true location of

the peaks (the truth) is the generator level charge-signed $1/P_{\rm T}$ of the $\mu^{\pm}$ after QED FSR, and they are denoted by $C^{\pm}_{\rm true}$. Thus, the calibration constraints for s and o are given by

$$C^{+}_{\rm true} = (1+s)\,C^{+} + o$$
$$C^{-}_{\rm true} = (1+s)\,C^{-} + o\,.$$

For the CDF calibration, muon pairs in the Z-boson region of $76 < M < 106$ GeV/c^2 are used. There are 262 thousand events in the sample, with very little background. The muons are binned using their (η, ϕ) trajectories: eight fixed-width ϕ bins and eight variable width η bins. The η bins span the region of -1.6 to 1.6, with bin boundaries of $-1,6$, -1.0, -0.6, -0.3, 0.0, 0.3, 0.6, 1.0, and 1.6. Unlike the LHC, the Tevatron $p\bar{p}$ collider has a broad luminous region along the beam line (30 cm rms). Consequently, the curvature peaks in many of the high η bins are not distinct. These bins contain significant numbers of both same-side (SS) and opposite-side (OS) muon pairs. The SS pairs have $\eta_1\eta_2 \geq 0$, where the subscript 1 (2) denotes Muon 1 (2). The OS pairs have $\eta_1\eta_2 < 0$. The peak of the $1/P_{\rm T}$ distribution of SS muon-pairs is closer to zero than OS pairs. Therefore muons in all (η, ϕ) bins are further partitioned into SS and OS bins.

The momentum scale calibration is iterative because the s and o calibration parameters affect the shape and location of the peaks. For the high η bins, the calibration accuracy is no better than 1% due to the limited number of calibration events. After the third iteration with curvature peaks, the more well defined Z-boson peak within the muon-pair invariant mass distribution determines the s and o calibration parameters. The final three iterations use the mass peaks. For the calibration using the muon-pair invariant mass peaks, one muon is selected as the tag leg which determines the bin. The second muon leg can be anywhere.

The momentum scale calibration is applied to both the data and simulated data. Bins that are perfectly calibrated have the correction values $s = 0$ and $o = 0$. The corrections for the data are much larger than those for the simulated data. In addition, corrections for the high $|\eta|$ bins are also larger than those for the central region bins. For the data, the rms of the scale correction (s) from the 128 calibration bins is 0.4%. The corresponding rms for the alignment offset correction (o) is 0.0003 $(\text{GeV}/c)^{-1}$, or 1.4% at $P_{\rm T} = M_Z/2$. The calibration of both the data and simulated data sets their absolute momentum scales to the common scale of the generator level $C_{\rm true}$ (after QED FSR).

The momentum resolution for the simulated data is calibrated to the momentum resolution of the data after the scale calibrations. The resolution calibration uses the initial curvature of the simulated data, C. The bias of this curvature relative to its true value for each event is

$$\Delta C_{\rm true} = C_{\rm true} - C\,.$$

The resolution is modified by changing the amount of bias on an event-by-event basis with the parameter f,

$$C' = C - f\,\Delta C_{\rm true}\,,$$

where C' is the new curvature. Relative to the original C distribution, the rms of the C' distribution is changed by the factor $1 + f$. This method is inappropriate for large values of f. The mass distributions of muon pairs in the $86 - 96$ GeV/c^2 region of the data and simulated data are used to determine f. The value which provides the best match to the data is $+0.15$, and the χ^2 of the simulated-data to data comparison is 68 over 79 bins.

The momentum scale and resolution calibrations depend on the agreement between the simulated data and data distributions for the muon $P_{\rm T}$ and invariant mass of the pair. The full results of the momentum scale and resolution calibration are presented in the next section which describes the data-driven corrections to the simulation.

C. Data Simulation Corrections

The data simulation presented in Sec. VI does not describe the data accurately enough for the $A_{\rm fb}$ measurement. Additional corrections applied to the simulated data are described in this section. All corrections are scale factors, or event weights, that are applied to simulated events. Both the data and simulated data are organized into 39 time periods for calibration purposes.

The first set of corrections are event-wide corrections. The event selections described in Sec. V are applied to both the data and simulated data. For each muon-pair topology (Sec. V C), the number of events is adjusted period-by-period to match the data. This adjustment contains corrections to the integrated luminosity, the trigger efficiency, and global reconstruction efficiencies for each muon-pair topology. The distributions of the number of $p\bar{p}$ collision vertices in each event (nVtx) and the location of these vertices along the beam-line (zVtx) changed significantly with improvements to the Tevatron collider. These distributions are inadequately simulated. The nVtx distibution is corrected on a period-by-period basis. The zVtx correction is split into a smaller set of seven correction blocks.

The momentum scale calibration described in the previous section is applied to both the data and the simulated data. The momentum resolution of the simulated data is then adjusted to match the resolution of the data. After these calibrations, the muon-pair invariant mass distribution of the simulated data is in good agreement with the data. The mass distributions are shown in Figs. 3 and 4. The muon $P_{\rm T}$ distributions are shown in Figs. 5 and 6.

As the Collins-Soper $\cos\vartheta$ distribution is important for corrections to the $A_{\rm fb}$ measurement, the simulated $\cos\vartheta$ distribution is adjusted to improve its agreement with

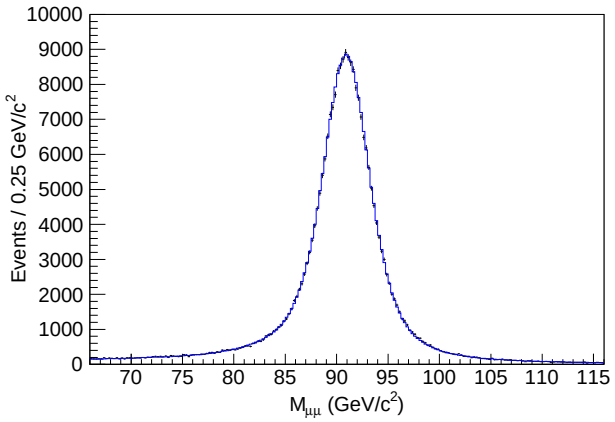

FIG. 3. Calibrated muon-pair invariant mass distributions. The crosses are the background-subtracted data, and the solid histogram is the simulation. The comparison of the simulation with the data yields a χ^2 of 219 for 200 bins.

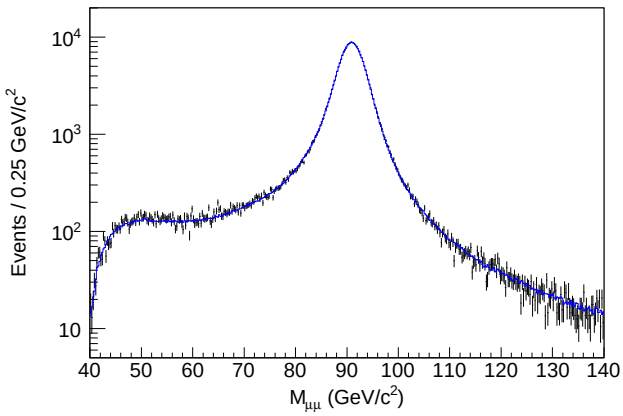

FIG. 4. Calibrated muon-pair invariant mass distributions. The crosses are the background-subtracted data, and the solid histogram is the simulation. The comparison of the simulation with the data yields a χ^2 of 518 for 400 bins.

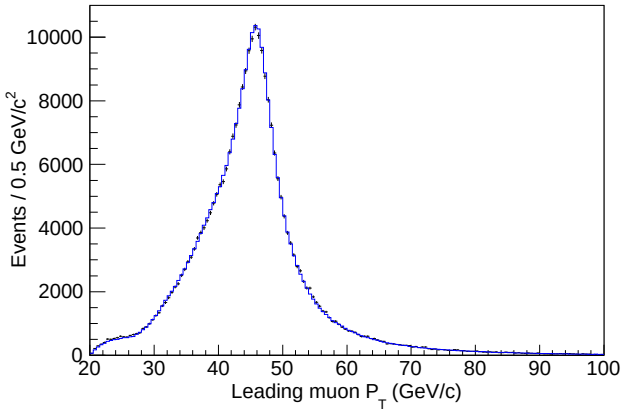

FIG. 5. Calibrated $P_{\rm T}$ distribution for the muon with the largest $P_{\rm T}$. The crosses are the background-subtracted data, and the solid histogram is the simulation.

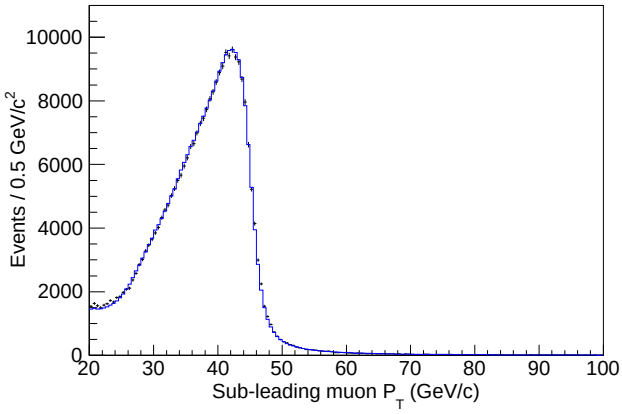

FIG. 6. Calibrated $P_{\rm T}$ distribution for the muon with the smallest $P_{\rm T}$. The crosses are the background-subtracted data, and the solid histogram is the simulation.

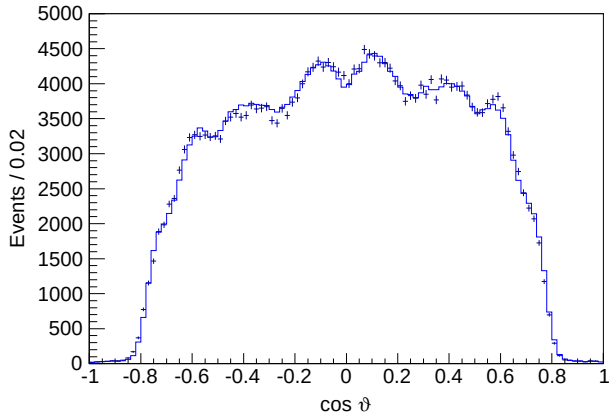

FIG. 7. The adjusted $\cos\vartheta$ distribution in the Collins-Soper frame. The crosses are the background-subtracted data, and the solid histogram is the simulation.

the data. The adjustments, determined for eight muon-pair invariant mass bins whose boundaries are aligned with those used in the measurement, are determined from the ratios of the data to simulated-data $\cos\vartheta$ distributions. These ratios are described well by the symmetric function $p_0 + p_2\cos^2\vartheta$, where p_0 and p_2 are parameters. The parametrized ratios are normalized to preserve the event count for the mass bin. The adjustment for the bin containing the Z-pole is uniform in $\cos\vartheta$. In bins away from the Z-pole, the adjustments redistribute events from the periphery of the $\cos\vartheta$ distribution to its center ($\cos\vartheta \sim 0$), but do not change the intrinsic asymmetries. With increasing distances of the mass bin from the Z-pole, the redistributions increase, but remain under 5%. The $\cos\vartheta$ distribution after the adjustments is shown in Fig. 7. The default φ distribution is adequate and is shown in Fig. 8.

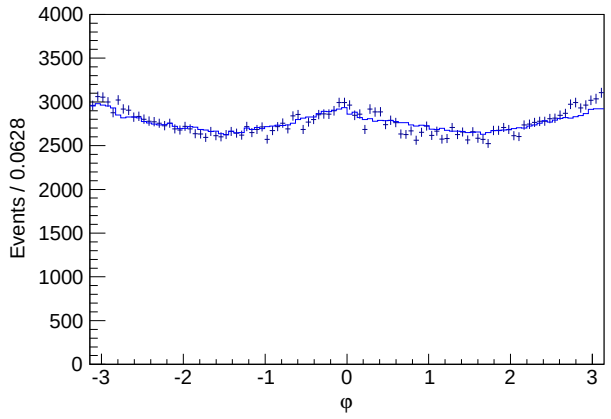

FIG. 8. The observed φ distribution in the Collins-Soper frame. The crosses are the background-subtracted data, and the solid histogram is the simulation.

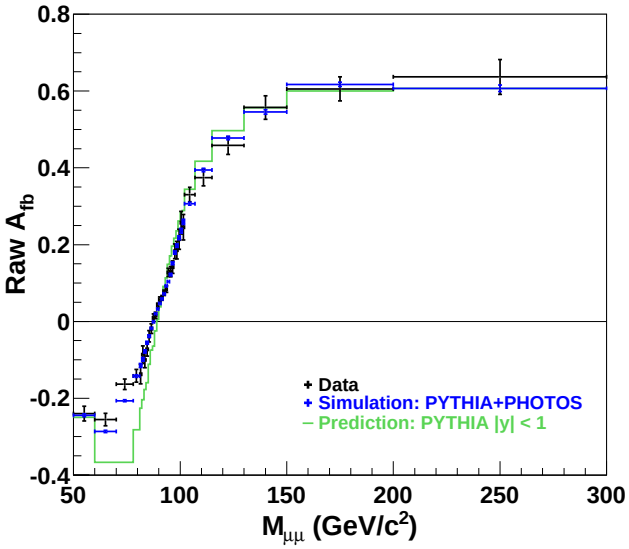

FIG. 9. The raw $A_{\rm fb}$ measurement in bins of the muon-pair invariant mass. Only statistical uncertainties are shown. The PYTHIA $|y| < 1$ asymmetry is before the addition of QED FSR.

D. Resolution Unfolding

After the calibrations and corrections to the data and simulated data, the raw $A_{\rm fb}$ is measured in bins of the muon-pair invariant mass with the event-weighting method. The measurement is shown in Fig. 9. The event-weighting method provides a first order acceptance correction, but without resolution unfolding.

Resolution unfolding uses the event transfer matrices from the simulation, denoted by $\bar{n}_{gr}$. They are the number of selected events that are generated in the muon-pair $(M, \cos\vartheta)$ bin g and reconstructed in the $(M, \cos\vartheta)$ bin r. Sixteen mass bins are defined. Their boundaries are: 50, 80, 82, 84, 86, 88, 89, 90, 91, 92, 93, 94, 96, 98, 100, 102, and 1000 GeV/c^2. The 50–80 and 102–1000 GeV/c^2 bins are referenced as the underflow and overflow bins, respectively. The forward-backward asymmetry has two angular states $\cos\vartheta \geq 0$ (+) and $\cos\vartheta < 0$ (−). Operationally, 32×32 square transfer matrices for a 32-element state vector are implemented. The first 16 elements of the vector are the mass bins for the + angular state, and the remaining 16 elements are for the − angular state.

The simulation predicts significant mass-bin to mass-bin event migration when the produced and reconstucted angular states are the same. There is very little migration of events from one angular state to the other. As the integrated luminosity of the simulation is normalized to the integrated luminosity of the data, the transfer matrices provide properly normalized estimates of event migration between bins. An estimator to the true unfolding matrix is $\bar{U}_{gr} = \bar{n}_{gr}/\bar{N}_r$, where $\bar{N}_r = \sum_g \bar{n}_{gr}$ is the expected total number of weighted events reconstructed in bin r. The 32-element state vector for $\bar{N}_r$ is denoted as $\vec{N}_r$, and the matrix $\bar{U}_{gr}$ by $\boldsymbol{U}$. The estimate for the resolution unfolded state vector of produced events is $\vec{N}_g = \boldsymbol{U} \cdot \vec{N}_r$. The accuracy of the simulation of $\boldsymbol{U}$ is determined by the statistics of the data.

For the event-weighting method, there are two transfer matrices that correspond to the weighted event counts N_n and N_d of Eqn. (5), and thus two separate unfolding matrices $\boldsymbol{U}$ and two separate event-weighted measurements of $\vec{N}_r$. They are used to estimate the two resolution unfolded $\vec{N}_g$ vectors from which $A_{\rm fb}$ is derived. The measurements of $A_{\rm fb}$ for the 16 mass bins are collectively denoted by $\vec{A}_{\rm fb}$.

The covariance matrix of the $A_{\rm fb}$ measurement is calculated using the unfolding matrices, the expectation values of $\vec{N}_r$ and $\vec{A}_{\rm fb}$ from the simulation, and their fluctuations over an ensemble. The per-experiment flucutation to $\vec{N}_g$ is $\boldsymbol{U} \cdot (\vec{N}_r + \delta\vec{N}_r)$, where $\delta\vec{N}_r$ represents a fluctuation from the expectation $\vec{N}_r$. The variation $\delta\vec{A}_{\rm fb}$ resulting from the $\vec{N}_g$ fluctuation is ensemble averaged to obtain the covariance matrix

$$\mathbf{Cov}_{\,lm} = \langle\, (\delta\vec{A}_{\rm fb})_l (\delta\vec{A}_{\rm fb})_m \,\rangle\,.$$

Each element i of $\vec{N}_r$ receives independent normally distributed fluctuations with an $(\text{rms})^2$ of $\bar{N}_i$. The two $\vec{N}_r$ vectors, the numerator vector and the denominator vector, have correlations. Element i of the numerator and denominator vectors contain the same events; the only difference is that they have different event weights. To include this correlation, the event-count variations of element i of the numerator and denominator $\delta\vec{N}_r$ vectors are based on the same fluctuation from a normal distribution with a unit rms.

The covariance matrix **Cov** is expanded and inverted to the error matrix using matrix singular value decomposition (SVD) methods. As the covariance matrix is real valued and a square 16×16 matrix, its 16 eigenvalues and eigenvectors are the rank-1 matrix components

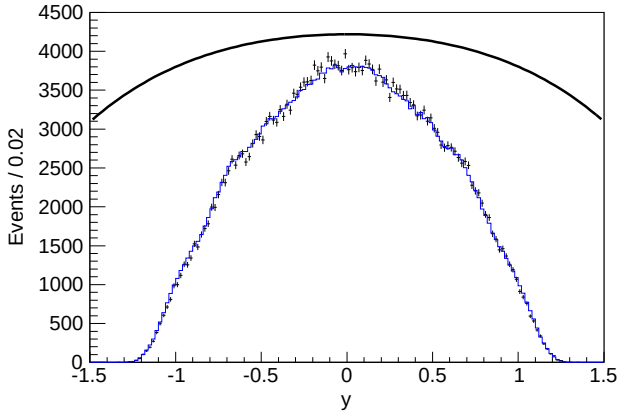

FIG. 10. The muon-pair y distribution. The crosses are the background-subtracted data and the histogram is the simulated data. The upper curve is the (arbitrarily normalized) shape of the underlying rapidity distribution from PYTHIA.

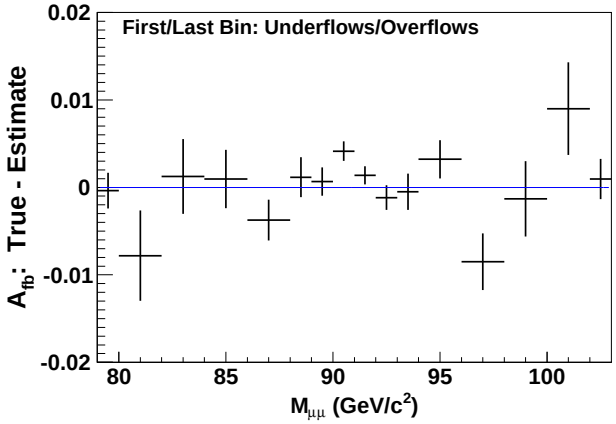

FIG. 11. The event-weighting bias for each of the muon-pair invariant mass bins. The bias is estimated with the simulation, and the uncertainties represent the full precision of the simulation. There is a net positive bias (0.0009 ± 0.0005), and this is expected due to the limited acceptance at the edges of the $|y| < 1$ measurement region for muon pairs.

in the decomposition of the covariance matrix and the error matrix:

$$\mathbf{Cov} = \sum_n \sigma_n \, (\vec{v}_n \vec{v}_n) \text{ and}$$
$$\mathbf{Cov}^{-1} = \sum_n \sigma_n^{-1} \, (\vec{v}_n \vec{v}_n) \, ,$$

where σ_n and $\vec{v}_n$ are the eigenvalues and eigenvectors of **Cov**, respectively, and $(\vec{v}_n \vec{v}_n)$ represents a vector projection operator, i.e., $|v_n\rangle\langle v_n|$ in the style of Dirac bra-kets.

The covariance matrix has several eigenvalues with very small values. They can be interpreted as simulation noise. While their terms contribute very little to the structure of the covariance matrix, they completely dominate the error matrix. Consequently, comparisons between the $A_{\rm fb}$ measurement and predictions that use the error matrix are unstable. An SVD method to attenuate this instablility is used, and presented in Sec. VIII.

E. Event-Weighting Bias Correction

After resolution unfolding, the event-weighted $A_{\rm fb}$ can have second-order acceptance and reconstruction efficiency biases. The most significant is the measurement bias from regions of limited or vanishing boson acceptance, and to a lesser extent, from detector non-uniformities ($(\epsilon A)^+ \neq (\epsilon A)^-$). The limited rapidity acceptance of muon pairs is shown in Fig. 10. As $|y|$ increases, $A_{\rm fb}$ slowly increases, and this increase is not fully accounted in the regions of limited or vanishing boson acceptance.

The bias is defined as the difference between the true value of $A_{\rm fb}$ calculated from the underlying events generated by PYTHIA and the simulation estimate. The estimate is the event-weighted simulated data $A_{\rm fb}$ after resolution unfolding. Kinematic distributions of the simulated data that are important for the unfolding matrix are adjusted to agree with the data, but the adjustments exclude terms linear in the $\cos\vartheta$ kinematic variable; the bias is specific to the intrinsic asymmetry of the simulation. The bias is a mass-bin by mass-bin additive correction to the unfolded $A_{\rm fb}$ measurement, and is shown in Fig. 11. The fully corrected measurement of $A_{\rm fb}$, which includes the bias correction, is shown in Fig. 12.

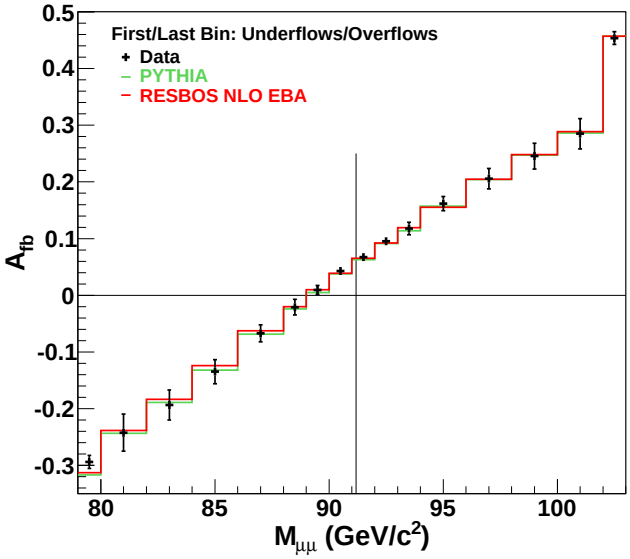

FIG. 12. The fully corrected $A_{\rm fb}$. The measurement uncertainties are uncorrelated bin-by-bin unfolding estimates. The vertical line is $M_{\mu\mu} = M_Z$. The PYTHIA calculation uses $\sin^2\theta^{\rm lept}_{\rm eff} = 0.232$. The EBA-based RESBOS calculation uses $\sin^2\theta_W = 0.2233$ ($\sin^2\theta^{\rm lept}_{\rm eff} = 0.2315$).

VIII. EXTRACTION OF $\sin^2\theta_{\rm eff}^{\rm lept}$

The EWK mixing parameter $\sin^2\theta_{\rm eff}^{\rm lept}$ ($\sin^2\theta_W$) is extracted from the $A_{\rm fb}$ measurement presented in Fig. 12 using a series of $A_{\rm fb}$ templates calculated using different values of $\sin^2\theta_W$. Three EBA-based calculations are used: LO (tree), RESBOS NLO, and POWHEG-BOX NLO. For the EBA electoweak form-factor calculations, the weak-mixing parameter is $\sin^2\theta_W$.

The $A_{\rm fb}$ measurement is directly sensitive to the effective-mixing parameters $\sin^2\theta_{\rm eff}$ which are combinations of the form factors and $\sin^2\theta_W$ (Sec. III A). The Drell-Yan $A_{\rm fb}$ is most sensitive to the effective-leptonic $\sin^2\theta_{\rm eff}^{\rm lept}$. While the extracted value of the effective-mixing parameters are independent of the details of the EBA model, the interpretation of the best-fit $\sin^2\theta_W$ and its corresponding form factors are dependent on the details of the EBA model.

The measurement and templates are compared using the χ^2 statistical measure evaluated with the $A_{\rm fb}$ measurement error matrix. A regularization term is added to the eigenvalue coefficients of the SVD expansion of the error matrix to attenuate the contributions of noise terms with small eigenvalues. The statistical uncertainties of the bias correction and the template calculation are used as uncorrelated regularization terms. Each uncertainty is projected onto the eigenvector basis of the covariance matrix then applied in quadrature as regularization terms:

$$\sigma_n \rightarrow \sigma_n + \sum_i (\vec{v}_n)_i^2 \Delta_i^2$$

where Δ_i is the uncertainty for mass bin i, and σ_n and $\vec{v}_n$ are the eigenvalue and eigenvector, respectively, of the covariance matrix basis vector n. Within the basis of the diagonal error matrix, all additional uncertainties are combined in quadrature with the measurement uncertainty.

Each template provides a scan point for the χ^2 function: $(\sin^2\theta_W, \chi^2(\sin^2\theta_W))$. The scan points are fit to a generic χ^2 functional form:

$$\chi^2(\sin^2\theta_W) = \bar{\chi}^2 + (\sin^2\theta_W - \overline{\sin}^2\theta_W)^2/\bar{\sigma}^2\,,$$

where $\bar{\chi}^2$, $\overline{\sin}^2\theta_W$, and $\bar{\sigma}$ are parameters. The $\overline{\sin}^2\theta_W$ parameter is the extracted (best-fit) value of $\sin^2\theta_W$ and $\bar{\sigma}$ the corresponding measurement uncertainty. The $\bar{\chi}^2$, relative to 16 mass bins, is the χ^2 goodness-of-fit for the extracted value.

The χ^2 distribution of the scan over templates from the RESBOS NLO calculation is shown in Fig. 13. The RESBOS EBA-based NLO QCD calculations of $A_{\rm fb}$ gives the default extracted value of $\sin^2\theta_W$. The results of the template scans are summarized in Table II. Included in the table for comparison are two other measurements: the CDF 2.1 fb^{-1} ee-pair A_4 result [5], and standard model Z-pole fits from LEP-1 and SLD [7].

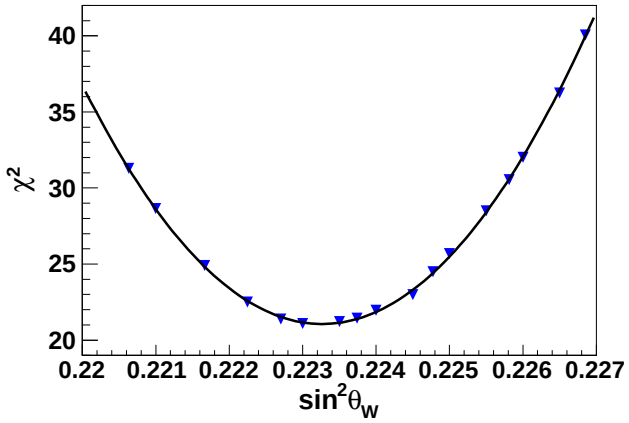

FIG. 13. Comparison of the $A_{\rm fb}$ measurement with the RESBOS NLO templates. The triangles are the scan points, and the solid curve is the fit of those points to a generic χ^2 functional form.

TABLE II. Extracted values of $\sin^2\theta_{\rm eff}^{\rm lept}$ ($\sin^2\theta_W$) for the EBA-based QCD templates. The PYTHIA entry is the value from the scan over non-EBA templates calculated by PYTHIA 6.4 with CTEQ5L PDFs. The uncertainties of the template scans are the measurement uncertainties ($\bar{\sigma}$). Also listed in parentheses are other measurements.

Template (Measurement)	$\sin^2\theta_{\rm eff}^{\rm lept}$	$\sin^2\theta_W$	$\bar{\chi}^2$
RESBOS NLO	0.2315 ± 0.0009	0.2233 ± 0.0008	21.1
POWHEG-BOX NLO	0.2314 ± 0.0009	0.2231 ± 0.0008	21.4
Tree LO	0.2316 ± 0.0008	0.2234 ± 0.0008	24.2
PYTHIA	0.2311 ± 0.0008	–	20.8
(CDF A_4)	0.2328 ± 0.0010	0.2246 ± 0.0009	–
(LEP-1+SLD)	0.23152 ± 0.00016	–	–

IX. SYSTEMATIC UNCERTAINTIES

The systematic uncertainties on the measurement of the effective-leptonic $\sin^2\theta_{\rm eff}^{\rm lept}$ and the inference of $\sin^2\theta_W$ (or M_W) contain contributions from both the measurement of $A_{\rm fb}$ and the template predictions of $A_{\rm fb}$ for various input values of $\sin^2\theta_W$. Both the experimental and prediction systematic uncertainties are small compared to the the experimental statistical uncertainty. The $A_{\rm fb}$ templates from POWHEG-BOX EBA-based NLO QCD calculations are used to estimate systematic uncertainties on the $\sin^2\theta_W$ parameter from various sources.

A. Measurement

The uncertainties considered are from the momentum scale and from the background estimates. The uncertainty from the backgrounds is the largest systematic uncertainty of the data. The total measurement systematic uncertainty is $\Delta\sin^2\theta_W = 0.00011$.

The momentum scale of both the data and simulated data are calibrated with the same technique to the same target scale. The absolute scale of the target is included in the measurement corrections. A combination of the resolution unfolding and the event-weighting bias correction tracks and accomodates the state of the absolute scale. However, a relative shift between the data and simulated data momentum scales is not accounted. The global muon momentum scale of the data is varied to determine the relative shifts allowed by the Z-pole mass peaks in the muon-pair invariant-mass distributions of the data and the simulated data. The scale shift is well constrained by the precision of the data in the 66–116 GeV/c^2 mass range (Fig. 3). The systematic uncertainty from the momentum scale is $\Delta \sin^2\theta_W = \pm 0.00005$.

Overall, the fraction of the backgrounds from EWK sources with their default integrated luminosity normalizations is 0.53%. In the low muon-pair invariant mass region, the level is $\sim 5\%$, and the simulated event yield in this region is a small amount less than the background subtracted data. An increase in the EWK background normalization of 60% can accomondate this small difference. This normalization shift is taken as the systematic uncertainty of the background normalization, and it yields $\Delta \sin^2\theta_W = \pm 0.00010$.

B. Predictions

The QCD mass-factorization and renormalization scales and uncertainties in the CT10 PDFs affects the $A_{\rm fb}$ templates. As the RESBOS calculation is chosen for use as the default $A_{\rm fb}$ templates, the associated uncertainty is also included in the overall systematic uncertainty. For the evaluation of the systematic uncertainties, the simulation equivalent of the $A_{\rm fb}$ measurement is used in template scans.

Instead of calculating the series of $A_{\rm fb}$ templates with different input values of $\sin^2\theta_W$ for each change of a QCD parameter, a simpler method is used. The $\sin^2\theta_W$ parameter is fixed to 0.2233 for all changes of QCD parameters. The predicted $A_{\rm fb}$ for the mass bin M with default QCD parameters is denoted by $\bar{A}_{\rm fb}(M, {\rm def})$, and when QCD parameter i is shifted, it is denoted by $\bar{A}_{\rm fb}(M, i)$. Each $\sin^2\theta_W$ scan point template is offset with the difference

$$A_{\rm fb}(M) \rightarrow A_{\rm fb}(M) + (\bar{A}_{\rm fb}(M, i) - \bar{A}_{\rm fb}(M, {\rm def}))\,.$$

The modified templates are then used in template scans for the best-fit value of $\sin^2\theta_W$. As there are no correlations of $A_{\rm fb}$ values among the mass bins, the uncorrelated χ^2 statistical measure is used for comparisons with the templates.

In all QCD calculations, the mass-factorization and renormalization scales are both set to the muon-pair invariant mass. To evaluate the effects of different scales, the running scales are varied independently by a factor ranging from 0.5 to 2 in the calculations. The largest observed deviation of the best-fit value of $\sin^2\theta_W$ from the default value is the QCD-scale uncertainty. This uncertainty is $\Delta \sin^2\theta_W({\rm QCD\ scale}) = \pm 0.00003$.

The PDF uncertainties are evaluated using the CT10 uncertainty PDFs which are from a global analysis of experimental data that utilizes 26 parameters and an associated error matrix in fits to the data. The uncertainty PDFs are 90% C.L. excursions from the best-fit parameters along the positive and negative directions of each error-matrix eigenvector. For the eigenvector i, the difference between the best-fit value of $\sin^2\theta_W$ for the positive (negative) direction uncertainty PDF and the best global-fit PDF value is denoted as $\delta_i^{+(-)}$. The 90% C.L. uncertainty for $\sin^2\theta_W$ is given by the following expression $\frac{1}{2}\sqrt{\sum_i (|\delta_i^+| + |\delta_i^-|)^2}$, where the sum i runs over the 26 eigenvectors. This value is scaled down by a factor of 1.645 for the 68% C.L. (one standard-deviation) uncertainty: $\Delta \sin^2\theta_W({\rm PDF}) = \pm 0.00036$.

The RESBOS $A_{\rm fb}$ templates are the default templates for the extraction of $\sin^2\theta_{\rm eff}^{\rm lept}$. The scan with the POWHEG-BOX or the tree templates yield slighty different values for $\sin^2\theta_W$ relative to the value from the RESBOS scan. The difference, denoted as the EBA uncertainty, is $\Delta \sin^2\theta_W({\rm EBA}) = \pm 0.00012$. Although the RESBOS and POWHEG-BOX predictions are fixed-order NLO QCD calculations at large boson $P_{\rm T}$, they are all-orders resummation calculations in the low-to-moderate $P_{\rm T}$ region which provides most of the total cross section. The EBA uncertainty is a combination of differences between the resummation calculations and the derived value of $\sin^2\theta_W$ with and without QCD radiation.

In summary, the total systematic uncertainties from the QCD mass-factorization and renormalization scales, and from the CT10 PDFs is ± 0.00036. All component uncertainties are combined in quadrature. With the inclusion of the EBA uncertainty, the total prediction uncertainty is ± 0.00038.

X. RESULTS

The values for $\sin^2\theta_{\rm eff}^{\rm lept}$ and $\sin^2\theta_W$ (M_W) extracted from the measurement of $A_{\rm fb}$ using $\mu^+\mu^-$ pairs from a sample corresponding to 9.2 fb^{-1} are

$$\begin{aligned}
\sin^2\theta_{\rm eff}^{\rm lept} &= 0.2315 \pm 0.0009 \pm 0.0004 \\
\sin^2\theta_W &= 0.2233 \pm 0.0008 \pm 0.0004 \\
M_W\ ({\rm indirect}) &= 80.365 \pm 0.043 \pm 0.019\ {\rm GeV}/c^2\,,
\end{aligned}$$

where the first contribution to the uncertainties are statistical and the second systematic. All systematic uncertainties are included and combined in quadrature, and the sources and amount of the these uncertainties are summarized in Table III. The inferred result on $\sin^2\theta_W$ or M_W is dependent on the standard model context specified in Appendix A, but the $\sin^2\theta_{\rm eff}^{\rm lept}$ result is independent because of its direct relationship with $A_{\rm fb}$.

TABLE III. Summary of the systematic uncertainties on the extraction of the weak mixing parameters $\sin^2\theta_{\rm eff}^{\rm lept}$ and $\sin^2\theta_W$.

Source	$\sin^2\theta_{\rm eff}^{\rm lept}$	$\sin^2\theta_W$
Momentum scale	±0.00005	±0.00005
Backgrounds	±0.00010	±0.00010
QCD scales	±0.00003	±0.00003
CT10 PDFs	±0.00037	±0.00036
EBA	±0.00012	±0.00012

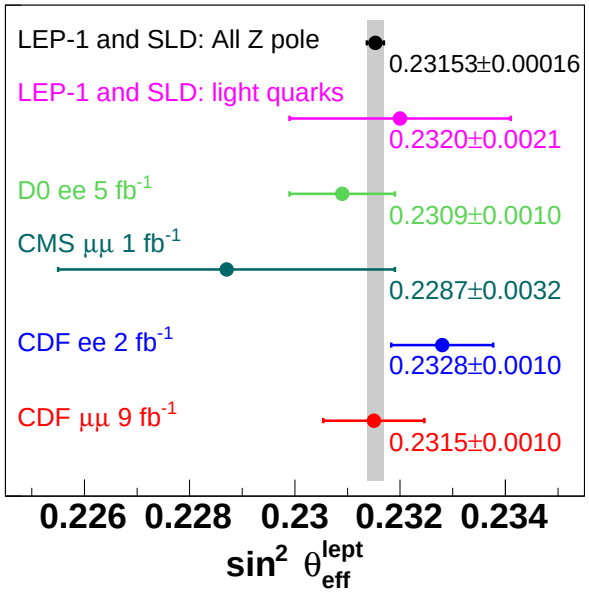

FIG. 14. Comparison of experimental measurements of $\sin^2\theta_{\rm eff}^{\rm lept}$: "All Z pole" represents the LEP-1 and SLD standard-model analysis of Z-pole measurements and "light quarks" represents the LEP-1 and SLD results from the light-quark asymmetries; "D0 ee 5 fb^{-1}" represents the D0 $A_{\rm fb}(M)$ analysis; "CMS $\mu\mu$ 1 fb^{-1}" represents the CMS multivariate analysis; "CDF ee 2 fb^{-1}" represents the A_4 analysis; and "CDF $\mu\mu$ 9 fb^{-1}" represents this analysis. The horizontal bars represent total uncertainties.

The measurement of $\sin^2\theta_{\rm eff}^{\rm lept}$ is compared with previous measurements from the Tevatron, LHC, LEP-1, and SLD. The Tevatron measurements are the D0 $A_{\rm fb}$ measurement based on 5 fb^{-1} of integrated luminosity [4], and the CDF measurement derived from the A_4 angular distribution coefficient of ee-pairs from a sample of 2.1 fb^{-1} of collisions [5]. The LHC measurement is the CMS multivariate analysis of Drell-Yan muon pairs from a sample of 1.1 fb^{-1} of integrated luminosity [6]. The LEP-1 and SLD measurements are from measurements at the Z-pole [7]. Figure 14 shows the comparisons. The total uncertainties of both CDF measurements include both the statistical and systematic uncertainties, which are combined in quadrature.

The W-boson mass inference is compared in Fig. 15 with previous direct and indirect measurements from the

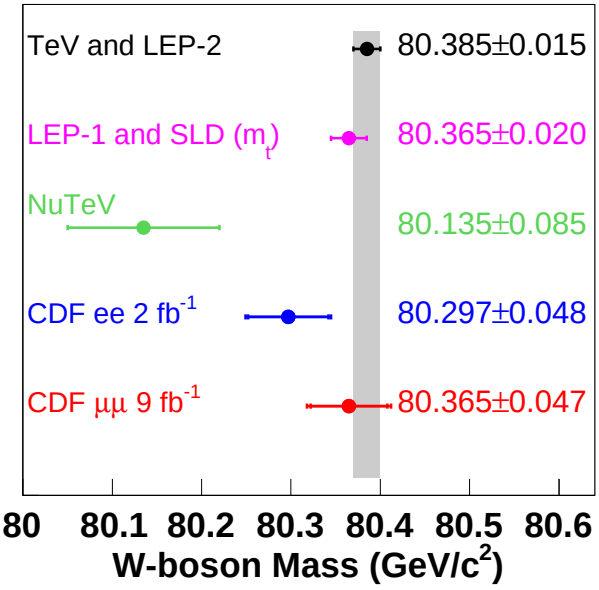

FIG. 15. Comparison of experimental determinations of the W-boson mass: "TeV and LEP-2" represents direct measurements of the W-boson mass; "LEP-1 and SLD (m_t)" represents the standard-model analysis of Z-pole measurements; "NuTeV" represents the indirect measurement derived from neutrino scattering at Fermilab; and "CDF ee 2 fb^{-1}" represents the A_4 analysis; and "CDF $\mu\mu$ 9 fb^{-1}" represents this analysis. The horizontal bars represent total uncertainties.

Tevatron, NuTeV, LEP-1, SLD, and LEP-2. The indirect measurement from the Tevatron collider is based on the A_4 angular coefficient analysis [5]. The indirect measurement from LEP-1 and SLD is from electroweak standard-model fits to Z-pole measurements in combination with the Tevatron top-quark mass measurement [42]. The NuTeV value, an indirect measurement, is based on the on-shell $\sin^2\theta_W$ parameter extracted from the measurement of the ratios of the neutral current to charged current ν and $\bar{\nu}$ cross sections at Fermilab [8]. The direct measurements are from the Tevatron and LEP-2 [43]. The total uncertainties of the two CDF inferences include both the statistical and systematic uncertainties, which are combined in quadrature. Both CDF analyses are indirect measurements of M_W, and they both use the same standard-model context for M_W.

XI. SUMMARY

The angular distribution of Drell-Yan letpon pairs provides information on the electroweak-mixing parameter $\sin^2\theta_W$. The muon forward-backward asymmetry in the polar-angle distribution $\cos\vartheta$ is governed by the $A_4\cos\vartheta$ term, whose A_4 coefficient is directly related to the $\sin^2\theta_{\rm eff}^{\rm lept}$ mixing parameter at the lepton vertex, and indirectly to $\sin^2\theta_W$. The effective-leptonic

$\sin^2\theta^{\rm lept}_{\rm eff}$ is derived from the measurement of the forward-backward asymmetry $A_{\rm fb}(M)$ based on a sample of muon pairs that correspond to 9.2 fb^{-1} of integrated luminosity from $p\bar{p}$ collisions at a center-of-momentum energy of 1.96 TeV. Calculations of $A_{\rm fb}(M)$ with different values of the electroweak-mixing parameter are compared with the measurement to determine the value of the parameter that best describes the measurement. The calculations include both quantum chromodynamic and electroweak radiative corrections. The best-fit values from the comparisons are summarized below.

$$\sin^2\theta^{\rm lept}_{\rm eff} = 0.2315 \pm 0.0010,$$
$$\sin^2\theta_W = 0.2233 \pm 0.0009, \text{ and}$$
$$M_W(\text{indirect}) = 80.365 \pm 0.047 \text{ GeV}/c^2 .$$

Each uncertainty includes statistical and systematic contributions. Both results are consistent with LEP-1 and SLD Z-pole measurements. The value of $\sin^2\theta^{\rm lept}_{\rm eff}$ are also consistent with the previous Tevatron values..

ACKNOWLEDGMENTS

We thank the Fermilab staff and the technical staffs of the participating institutions for their vital contributions. This work was supported by the U.S. Department of Energy and National Science Foundation; the Italian Istituto Nazionale di Fisica Nucleare; the Ministry of Education, Culture, Sports, Science and Technology of Japan; the Natural Sciences and Engineering Research Council of Canada; the National Science Council of the Republic of China; the Swiss National Science Foundation; the A.P. Sloan Foundation; the Bundesministerium für Bildung und Forschung, Germany; the Korean World Class University Program, the National Research Foundation of Korea; the Science and Technology Facilities Council and the Royal Society, United Kingdom; the Russian Foundation for Basic Research; the Ministerio de Ciencia e Innovación, and Programa Consolider-Ingenio 2010, Spain; the Slovak R&D Agency; the Academy of Finland; the Australian Research Council (ARC); and the EU community Marie Curie Fellowship Contract No. 302103.

Appendix A: ZFITTER

The input parameters to the ZFITTER radiative-correction calculation are particle masses, the electromagnetic fine-structure constant α_{em}, the Fermi constant G_F, the strong coupling at the Z mass $\alpha_s(M_Z^2)$, and the contribution of the light quarks to the "running" α_{em} at the Z mass $\Delta\alpha^{(5)}_{em}(M_Z^2)$ (DALH5). The scale-dependent couplings are $\alpha_s(M_Z^2) = 0.118$ and $\Delta\alpha^{(5)}_{em}(M_Z^2) = 0.0275$ [44]. The mass parameters are $M_Z = 91.1875$ GeV/c^2 [7], $m_t = 173.2$ GeV/c^2 (top quark) [42], and $m_H = 125$ GeV/c^2 (Higgs boson). Form factors and the Z-boson total-decay width Γ_Z, are calculated.

The renormalization scheme used by ZFITTER is the on-shell scheme [13], where particle masses are on-shell, and

$$\sin^2\theta_W = 1 - M_W^2/M_Z^2 \qquad \text{(A1)}$$

holds to all orders of perturbation theory by definition. If both G_F and m_H are specified, $\sin\theta_W$ is not independent, and is derived from standard-model constraints that use radiative corrections. To vary the $\sin\theta_W$ (M_W) parameter, the value of G_F is changed by a small amount prior to the calculation so that the derived M_W range is 80.0–80.5 GeV/c^2. The set of M_W values corresponds to a family of physics models with standard-model like couplings where $\sin^2\theta_W$ and the coupling (G_F) are defined by the M_W parameter. The Higgs-boson mass constraint $m_H = 125$ GeV/c^2 keeps the form factors within the vicinity of standard-model fit values from LEP-1 and SLD [7]. The primary purpose of ZFITTER is to provide tables of form factors for each model. Additional implementation details are provided in [5].

[1] S. D. Drell and T.-M. Yan, Phys. Rev. Lett. **25**, 316 (1970).
[2] J. Beringer *et al.* (Particle Data Group), Phys. Rev. D **86**, 010001 (2012).
[3] D. Acosta *et al.* (CDF Collaboration), Phys. Rev. D **71**, 052002 (2005).
[4] V. M. Abazov *et al.* (D0 Collaboration), Phys. Rev. D **84**, 012007 (2011).
[5] T. Aaltonen *et al.* (CDF Collaboration), Phys. Rev. D **88**, 072002 (2013).
[6] S. Chatrchyan *et al.* (CMS Collaboration), Phys. Rev. D **84**, 112002 (2011).
[7] S. Schael *et al.* (ALEPH, DELPHI, L3, OPAL, and SLD Collaborations, LEP Electroweak Working Group, and SLD Electroweak and Heavy Flavour Groups), Phys. Rept. **427**, 257 (2006).
[8] G. P. Zeller *et al.* (NuTeV Collaboration), Phys. Rev. Lett. **88**, 091802 (2002); **90**, 239902(E) (2003).
[9] A. Aktas *et al.* (H1 Collaboration), Phys. Lett. B **632**, 35 (2006).
[10] J. C. Collins and D. E. Soper, Phys. Rev. D **16**, 2219 (1977).
[11] E. Mirkes, Nucl. Phys. **B387**, 3 (1992); E. Mirkes and J. Ohnemus, Phys. Rev. D **50**, 5692 (1994).
[12] D. Bardin, M. Bilenky, T. Riemann, M. Sachwitz, and H. Vogt, Comput. Phys. Commun. **59**, 303 (1990); D. Bardin, P. Christova, M. Jack, L. Kalinovskaya, A. Olchevski, S. Riemann, and T. Riemann, **133**, 229 (2001); A. Arbuzov, M. Awramik, M. Czakon, A. Freitas, M. Grünewald, K. Monig, S. Riemann, and T. Riemann,

174, 728 (2006).
[13] A. Sirlin, Phys. Rev. D **22**, 971 (1980).
[14] H.-L. Lai, M. Guzzi, J. Huston, Z. Li, P. Nadolsky, J. Pumplin, and C.-P. Yuan, Phys. Rev. D **82**, 074024 (2010).
[15] G. A. Ladinsky and C.-P. Yuan, Phys. Rev. D **50**, R4239 (1994); C. Balàzs and C.-P. Yuan, **56**, 5558 (1997); F. Landry, R. Brock, P. M. Nadolsky, and C.-P. Yuan, **67**, 073016 (2003); A. Konychev and P. Nadolsky, Phys. Lett. B **633**, 710 (2006).
[16] S. Alioli, P. Nason, C. Oleari, and E. Re, J. High Energy Phys. **07**, 060 (2008).
[17] J. C. Collins, D. E. Soper, and G. Sterman, Nucl. Phys. **B250**, 199 (1985); J. C. Collins and D. E. Soper, **B193**, 381 (1981); **B197**, 446 (1982); **B213**, 545(E) (1983).
[18] P. M. Nadolsky *et al.* (CTEQ Collaboration), Phys. Rev. D **78**, 103004 (2008).
[19] T. Sjöstrand, S. Mrenna, and P. Z. Skands, J. High Energy Phys. **05**, 026 (2006).
[20] A. Abulencia *et al.* (CDF Collaboration), J. Phys. G: Nucl. Part. Phys. **34**, 2457 (2007).
[21] T. Affolder *et al.*, Nucl. Instrum. Methods Phys. Res., Sect. A **526**, 249 (2004).
[22] T. Aaltonen *et al.*, Nucl. Instrum. Methods Phys. Res., Sect. A **729**, 153 (2013).
[23] L. Balka *et al.*, Nucl. Instrum. Methods Phys. Res., Sect. A **267**, 272 (1988).
[24] S. Bertolucci *et al.*, Nucl. Instrum. Methods Phys. Res., Sect. A **267**, 301 (1988).
[25] M. Albrow *et al.*, Nucl. Instrum. Methods Phys. Res., Sect. A **480**, 524 (2002).
[26] G. Apollinari *et al.*, Nucl. Instrum. Methods Phys. Res., Sect. A **412**, 515 (1998).
[27] P. de Barbaro, IEEE Trans. Nucl. Sci. **42**, 510 (1995).
[28] G. Ascoli *et al.*, Nucl. Instrum. Methods Phys. Res., Sect. A **268**, 33 (1988).
[29] E. J. Thomson *et al.*, IEEE Trans. on Nucl. Sci. **49**, 1063 (2002).
[30] W. Ashmanskas *et al.*, Nucl. Instrum. Methods Phys. Res., Sect. A **518**, 532 (2004).
[31] L. Ristori and G. Punzi, Annu. Rev. Nucl. Part. Sci. **60**, 595 (2010).
[32] A. Adelman *et al.*, Nucl. Instrum. Methods Phys. Res., Sect. A **572**, 361 (2007).
[33] T. Sjöstrand, P. Edén, L. Lönnblad, G. Miu, S. Mrenna, and E. Norrbin, Comput. Phys. Commun. **135**, 238 (2001).
[34] H. L. Lai *et al.* (CTEQ Collaboration), Eur. Phys. J. C **12**, 375 (2000).
[35] T. Affolder *et al.* (CDF Collaboration), Phys. Rev. Lett. **84**, 845 (2000).
[36] M. Albrow *et al.* (Tev4LHC QCD Working Group), arXiv:hep-ph/0610012 [hep-ph].
[37] E. Barberio and Z. Was, Computer Phys. Comm. **79**, 291 (1994); E. Barberio, B. van Eijk, and Z. Was, **66**, 115 (1991).
[38] P. Golonka and Z. Was, Eur. Phys. J. C **45**, 97 (2006).
[39] A. Bodek, Eur. Phys. J. C **67**, 321 (2010).
[40] T. Aaltonen *et al.* (CDF Collaboration), Phys. Rev. Lett. **106**, 241801 (2011).
[41] A. Bodek, A. van Dyne, J.-Y. Han, W. Sakumoto, and A. Strelnikov, Eur. Phys. J. C **72**, 2194 (2012).
[42] T. Aaltonen *et al.* (CDF and D0 Collaborations), Phys. Rev. D **86**, 092003 (2012).
[43] T. Aaltonen *et al.* (CDF Collaboration and D0 Collaboration), Phys. Rev. D **88**, 052018 (2013).
[44] F. Jegerlehner, Nuovo Cim. C **034S1**, 31 (2011).